Determination of Pattern Allowances for a Distorted Steel Casting using an Inverse Elastoplastic Analysis

D. Galles,[1] J. Lu,[2] and C. Beckermann[2]

[1]Oak Ridge Associated Universities, Oak Ridge, TN 37830, USA
[2]Department of Mechanical Engineering, University of Iowa, Iowa City, IA 52242, USA

Abstract

In recent years, the development of computational models to predict casting distortions has led to improvements in efficiency and accuracy over traditional pattern design that relies on shrink rules. Unfortunately, the determination of pattern dimensions using simulation remains a trial-and-error process that requires several design iterations. In this study, the finite element inverse elastoplastic analysis is utilized to calculate the pattern geometry in a single iteration for a plastically deformed (i.e., distorted) body. A simple bar is analyzed first to show proof of concept. Then, a simplified casting system is simulated to demonstrate the feasibility of the inverse method for production castings. For each case, an inverse simulation is performed first to calculate the pattern shape. This configuration is then used as the input geometry for a forward simulation, which is shown to successfully recover the original as-cast shape used for the inverse analysis. Through this sequence, the inverse deformation method is shown to be a viable technique for the determination of pattern allowances in production castings.

1. Introduction

Casting distortions are unintended deformations that occur during metalcasting. Their presence, which creates dimensional inaccuracies in the as-cast part, is attributed to mechanical stresses, thermal stresses, or some combination of both. Mechanical stresses arise from contact interactions between the casting and mold (e.g., a sand core restrains thermal contractions in the casting), whereas thermal stresses are the result of uneven cooling in the casting and lead to spatially varying thermal strain rates. For both cases, permanent (i.e., plastic) deformations occur when stress levels exceed the yield strength of the casting material. As a result, feature dimensions may not adhere to customer specifications. For this reason, pattern design is inherently an iterative process for which the patternmaker alters the pattern through a trial-and-error process until the desired dimensions are achieved. For each iteration, a casting is produced and then evaluated through a dimensional analysis. Such a design strategy is not only expensive (due to the high energy costs associated with casting) but also time-consuming. Furthermore, the efficiency of the process heavily relies on the patternmaker's expertise, which can vary considerably.

In recent years, the remarkable increase in computer speeds has coincided with advancements in computational codes suitable for predicting stresses and distortions during casting. Such progress has paved the way for a paradigm shift from physically to digitally-based design within industry. Today's casting simulations can be performed with good accuracy and in a fraction of the time needed to produce and analyze a physical casting. As a result, considerable time and cost savings are realized. Moving forward, additional improvements in accuracy and efficiency can be expected to further increase the role computer simulation for pattern design.

Despite the benefits, digitally-based pattern design is similar to its physical counterpart in that both are iterative procedures. This is due to the fact that the kinematics

of finite element codes are typically implemented in a forward framework. In other words, the finite element simulations start from a reference configuration (i.e., pattern shape) and, based on the loading history, calculate the deformed configuration (i.e., as-cast shape). Hence, pattern design, whether physically or digitally-based, remains a trial-and-error approach whose efficiency is predicated on the expertise of the patternmaker/design engineer.

Pattern design belongs to a class of engineering applications in which the unknown reference geometry must be determined. To this end, Yamada [1] and Govindjee et al. [2] pioneered an inverse method that directly solves the equilibrium boundary condition for an elastic material. These seminal studies spurred the development of inverse finite element implementations that were capable of determining the reference configuration firstly for elastic deformations and later for elastoplastic deformations. A comprehensive review of the formulation for elastic deformation is given by Lu and Li [3]. Unfortunately, a caveat for the elastoplastic problem is that the deformations are history dependent and thus, the inverse deformation problem is generally ill-posed. A unique solution is only achieved when the loading history or the plastic strain in the deformed state is known, as demonstrated by Germain et al. [4]. The authors also proposed a recursive procedure wherein the deformation and plastic variables were determined separately through nested iterations of inverse and forward analyses [5]. Lu and Li [6] further demonstrated that an inverse boundary value problem gives reasonably accurate results for both displacement and plastic variables, provided the deformations are moderately large and the loading history is nearly monotonic. In general, casting processes can be expected to fall under these conditions, as 1) loading is predominantly driven by (nearly) monotonic cooling and 2) the associated thermal strains induce dimensional changes typically on the order of a few percent. An exception occurs during solid state phase transformations, when transformation-induced volumetric expansion may lead to unloading. However, the inverse solution will be applicable as long as minimal plastic deformations occur during the

transformation.

In this study, the direct approach of inverse analysis developed by Lu and Li [6] is utilized for plastically deformed (i.e., distorted) material bodies in order to determine pattern dimensions for a steel casting. A simple rectangular bar is analyzed first to demonstrate the feasibility of the technique. Then, elastoplastic deformations are calculated for a realistic casting geometry consisting of a steel plate outfitted with risers and a gating system. The desired as-cast shapes are shown Figure 1 and serve as inputs for the inverse analysis. The mold is excluded from the stress analyses in order to prevent numerical difficulties encountered with contact interactions between the casting and mold. Consequently, deformations in this study are induced exclusively by thermal stresses. For
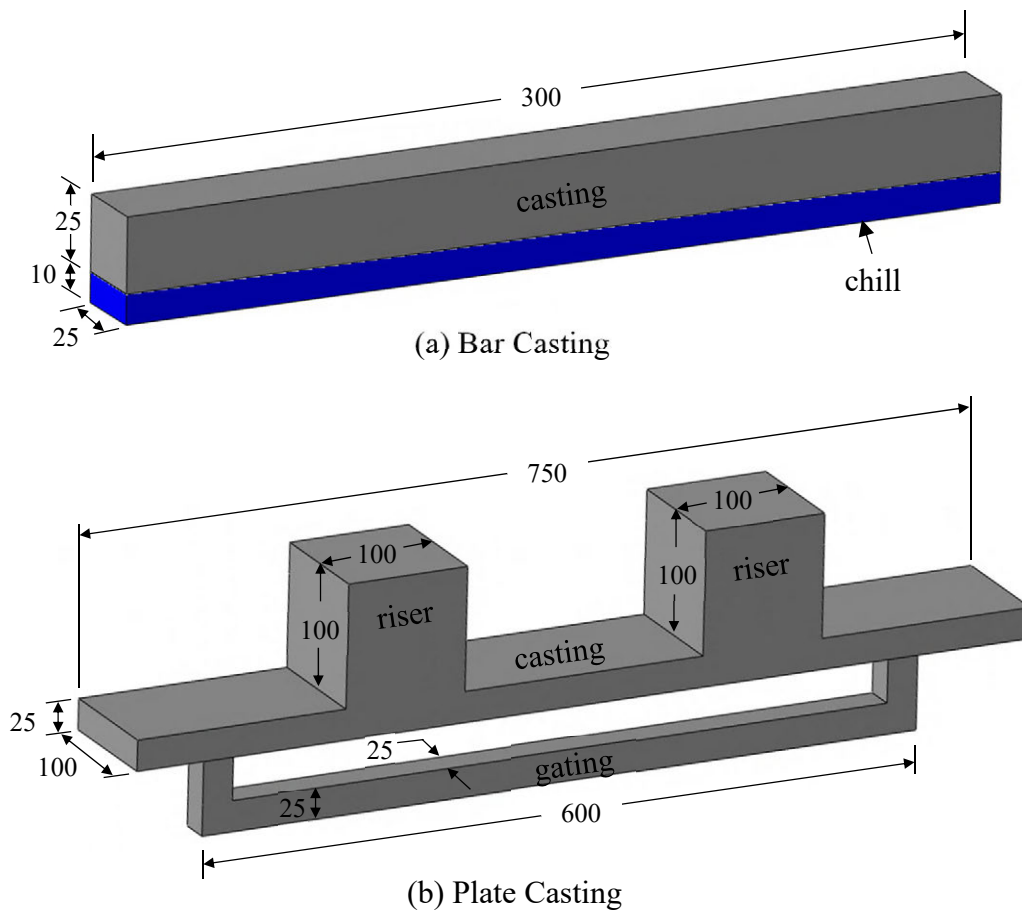

Figure 1. Geometries for the bar (a) and plate (b) castings. Dimensions in mm.

the simulations, a sequential thermal-mechanical analysis is performed in which the transient temperature fields are calculated first using casting simulation software and then used as inputs for the forward and inverse stress analyses. Loop tests are conducted for the analyses, in which the inverse problem is solved first to determine the pattern shape, which is subsequently used as the input geometry for the forward analysis. The inverse technique is evaluated by the forward problem's ability to recover the original geometry used for the inverse analysis. Finally, the accuracy of the inverse elastoplastic solution is evaluated through an error analysis.

2. Background and previous work on casting distortions

This work builds upon previous studies that have been performed over the past decade in the Solidification Laboratory at the University of Iowa. This section not only summarizes these studies but also provides the underlying motivation that demonstrates their necessity.

Computer simulation software used for the purpose of predicting casting distortions is widely available for today's casting engineer. In particular, the finite element method (FEM) is the preferred method used by commercial software companies (e.g., MAGMASOFT® [7]) to calculate stresses and distortions during casting. When used in this manner, an FEM simulation is commonly referred to as a stress analysis. FEM is a well-established and powerful technique that can be used to simulate casting processes in a fraction of the time and cost needed to produce and analyze a physical casting. Today's FEM software packages are also user-friendly and can be learned with minimal effort.

Despite these benefits, care must be taken in order to ensure the accuracy of the FEM simulations. For example, the constitutive (i.e., stress-strain) relations used in the computational model must consider all relevant physical phenomena that contribute to distortions. Failure to do so results in simplified models with limited predictive capabilities. Also, the simulations must utilize realistic material properties and constitutive model

parameters, which necessitates an extensive calibration procedure. This procedure typically involves performing experiments, in which measurements are taken during casting (i.e., in situ measurements). By doing so, the data inherently captures the effects of the harsh environment encountered during casting, which may not be possible in a laboratory setting. For this reason, model calibration using in situ measurements is preferable, as it will likely lead to better simulation accuracy than similar calibration with laboratory (i.e., ex situ) measurements. Once the experimental data has been collected, the experiments are simulated and the predictive capability of the simulation is evaluated based on its ability to recreate the experimental observations. Any disagreements between the simulation and experimental results are subsequently minimized through careful alterations to the computational model.

The large temperature range encountered during casting is also notable, as it influences the evolution of distortions in two ways. First, material properties vary with temperature. For example, the yield strength (σ_{yield}) of a low alloy casting is much greater at room temperature ($\sigma_{yield} \approx 300$ MPa) than it is at the solidus temperature ($\sigma_{yield} < 5$MPa). Thus, the magnitude of calculated distortions strongly depends on the temperature. Second, the accumulation of thermal strains during solidification and cooling is the driving factor that leads to mechanical and thermal stresses. Without thermal strains, castings would be distortion-free. For these reasons, the temperature histories of the casting and mold must be known prior to the FEM simulations. These can be determined by performing a heat transfer analysis, which calculates the temperatures at all times and locations during casting. The calculated transient temperature fields are then inputted into the stress analysis, which subsequently calculates stresses and distortions. This strategy, which is commonly referred to as a sequentially coupled thermal-mechanical stress analysis, was used for the studies described below. For each study, thermocouples were inserted in both the casting and mold in order to continuously record temperatures during the casting experiments. These measurements served as validation for the heat transfer simulations to

ensure that realistic temperature fields were used for the stress analysis.

The ultimate objective for this body of work was to calibrate a computational model that can accurately predict distortions during sand casting of ASTM A216 grade WCB steel. This was accomplished through separate studies that focused on the steel [8] and sand mold [9,10]. For the initial study, Galles and Beckermann [8] cast a steel bar in a sand mold to calibrate constitutive parameters for an elasto-visco-plastic model. A schematic of the experimental setup is shown in Figure 2. Using a restraint frame outfitted with a turnbuckle, an axial force was applied to the bar beginning near the end of solidification and continuing throughout cooling in order to induce distortions. The axial force and displacement were continuously measured with load bolts and LVDTs (Linear Variable Differential Transformers), respectively. In total, five experiments were performed. For each experiment, the applied axial force was varied with time and magnitude to create different loading histories, which in turn produced different amounts of distortions. The initial FEM simulations, for which constitutive model parameters were estimated using well-known data from the literature [11], generally under-predicted the distortions. Through an
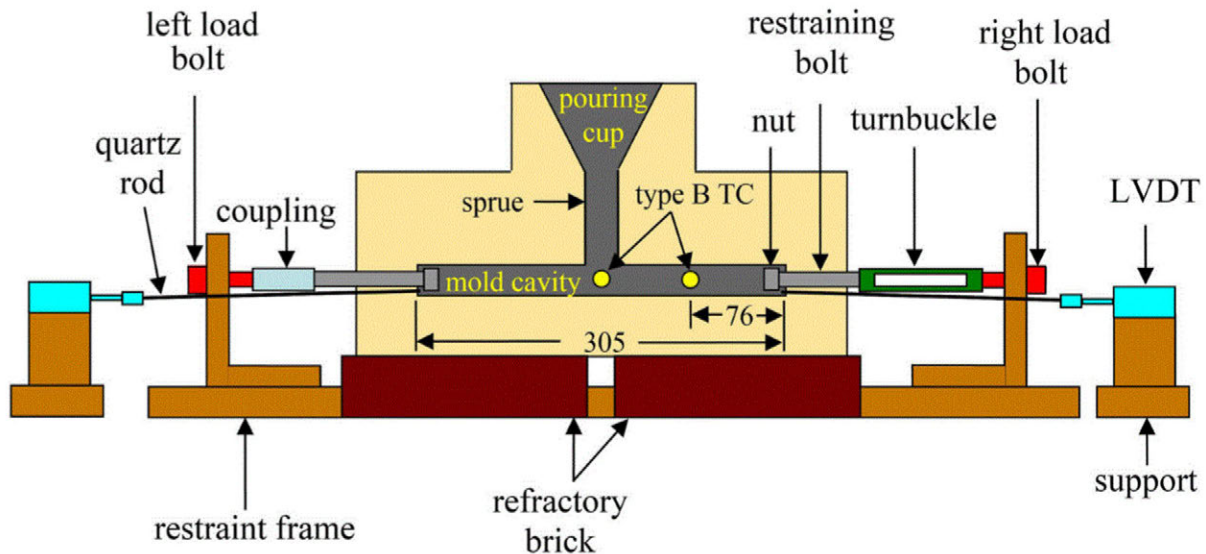

Figure 2. Schematic of the experimental setup for the strained bar experiments. Dimensions in mm.

adjustment to a single constitutive parameter (i.e., strain rate sensitivity exponent, m), the simulations successfully predicted the evolution of the observed deformations. An example of this adjustment procedure can be seen in Figure 3. For this experiment, the turnbuckle was engaged at approximately 200 s, which produced an axial force that increased the axial length from 200 s to 250 s (see the "measurement" curve in Figure 3(a)). Using model parameters estimated from [11], the initial simulation far under-predicted this deformation. After an adjustment to the strain rate sensitivity exponent, however, the simulation accurately predicted the observed evolution of the bar's axial length. The initial (i.e., estimated) and adjusted strain rate sensitivity exponents are shown in Figure 3(b). A final comparison between measured and predicted axial length changes for all experiments, as well as their corresponding adjusted strain rate sensitivity exponents, are shown in Figures 4(a) and 4(b), respectively. Using these adjusted strain rate sensitivity curves as a guide, a final representative curve was constructed.

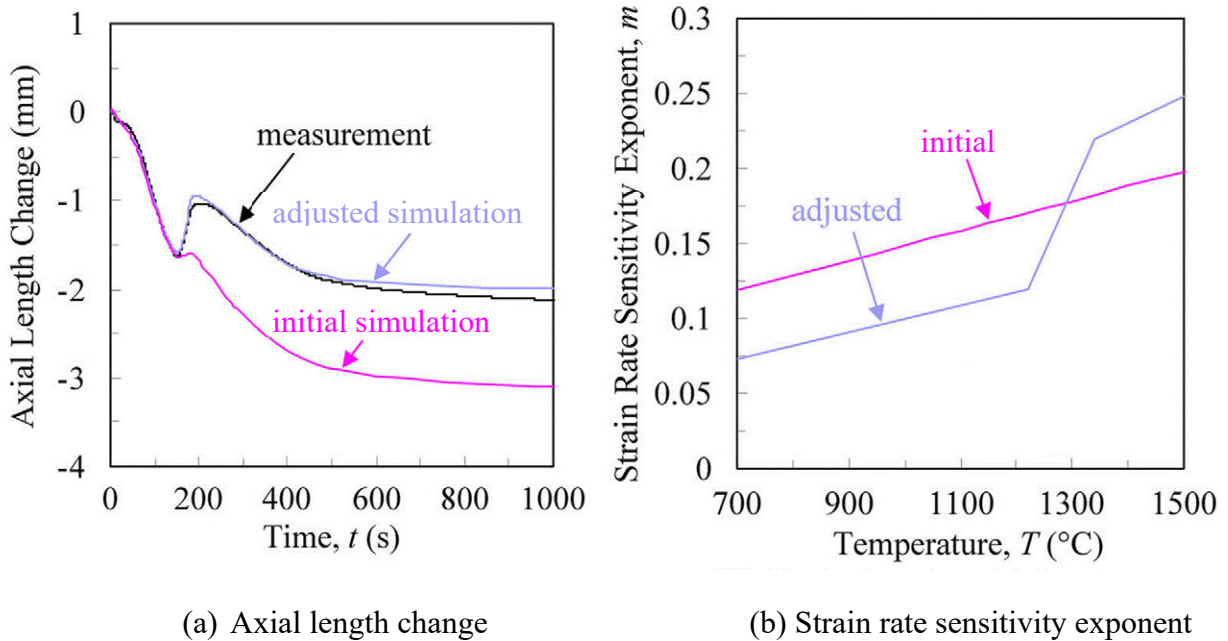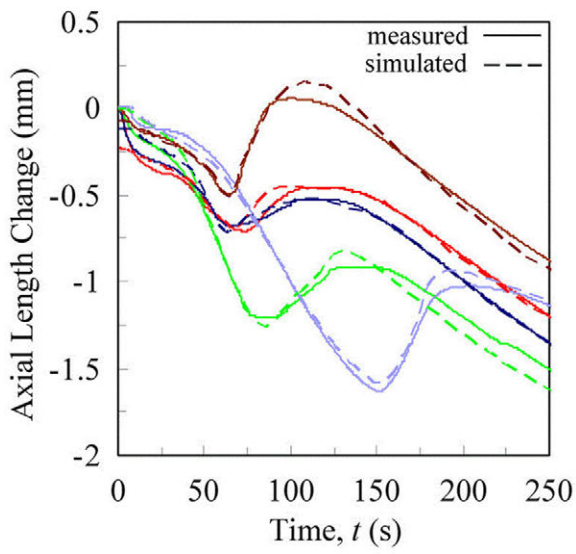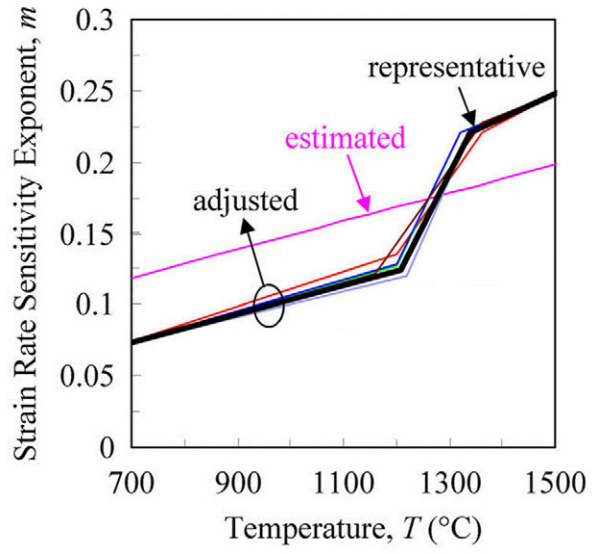(a) Axial length change   (b) Strain rate sensitivity exponent

Figure 3. Example of a comparison between measured and predicted changes in axial length (a). Variations in the simulation results are due to the different strain rate sensitivity exponents shown in (b).

(a) Axial length change

(b) Strain rate sensitivity exponent

Figure 4. Comparison between measured and simulated axial length changes for all experiments (a) when using the adjusted strain rate sensitivity exponents in (b).

Next, the mechanical behavior of the mold was investigated. Galles and Beckermann [9] utilized a core to cast a hollow steel cylinder in a sand mold. The casting geometry and experimental schematic are depicted in Figure 5. Separate experiments were
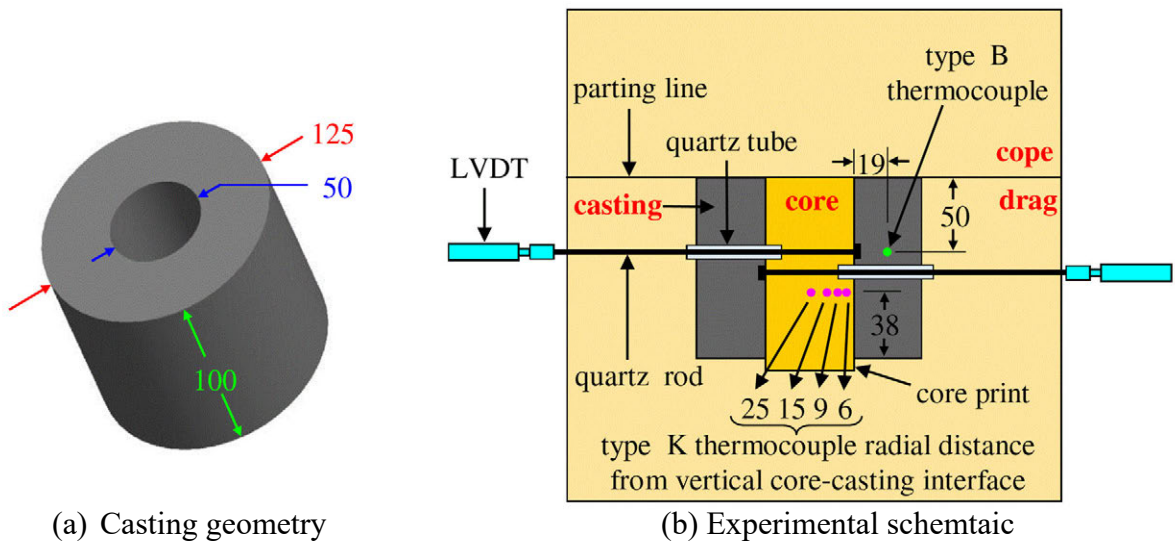
(a) Casting geometry

(b) Experimental schemtaic

Figure 5. Casting geometry (a) and experimental schematic (b) for the cylinder experiments. All dimensions are in mm.

conducted using silica and zircon core sands and each was repeated four times. Immediately after pouring, the core rapidly heated and expanded, causing an increase of the cylinder's inner diameter. The evolution of this expansion was measured at the cylinder's mid-height and is shown on complete and 600 s time scales in Figures 6(a) and 6(b), respectively. During the experiments that used bonded silica sand for the cores (see the family of red curves in Figure 6), the inner diameter increased by approximately 2 mm, which was roughly double the observed increase for the experiments that used zircon sand (blue curves). This discrepancy was attributed to large differences between the thermal expansion coefficients for the two sands. It was found that during the experiments, the cylinder's inner diameter only increased during solidification, after which the casting contained the sufficient strength to prevent any further core expansion. This behavior is illustrated by Figure 6(b), as the maximum change in inner diameter occurs prior to complete solidification. Any subsequent changes in the inner diameter were due to thermal
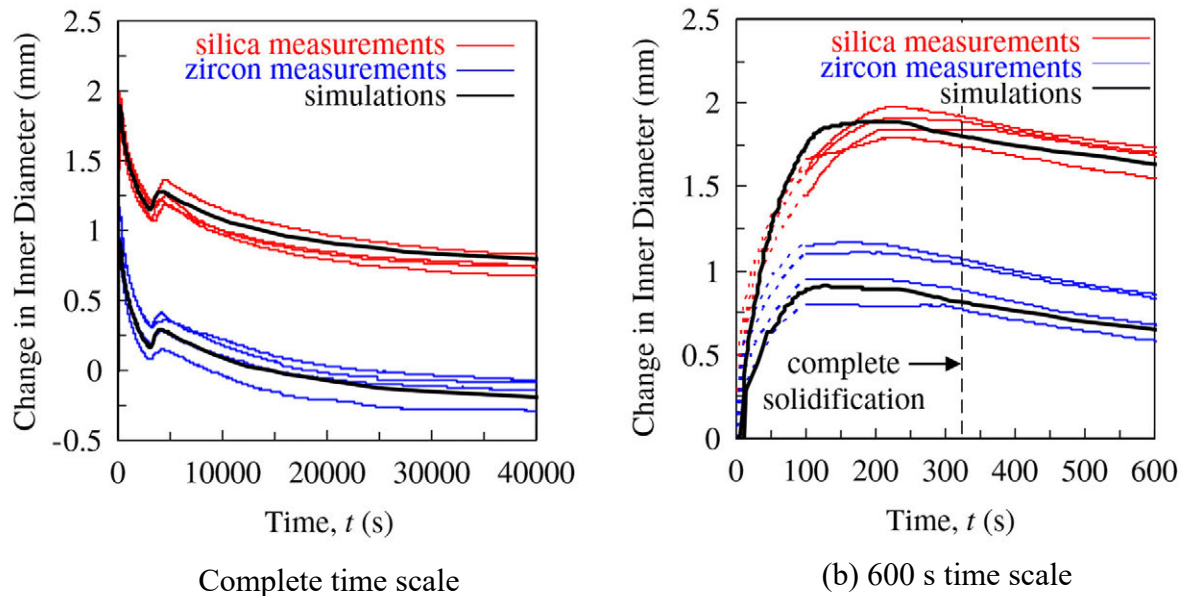

Figure 6. Comparison between measured and simulated axial length changes for all experiments (a) when using the adjusted strain rate sensitivity exponents in (b).

strains only; no distortions were measured after solidification. The initial FEM simulations revealed that thermal expansion of the core alone was insufficient to predict the observed core expansion. This prompted the authors to consider sand dilation, which is the volumetric expansion of the sand aggregate when subjected to shear stresses. Essentially, the voids between individual sand grains grow larger during dilation, which increases the total volume. This behavior is illustrated in Figure 7. After dilation was incorporated into the simulation model, the observed inner diameter expansion was accurately predicted, as shown by the black curves in Figure 6. In addition, the measured pattern allowances for the cylinder's inner diameter were also accurately predicted (see Figure 8). Notably, the largest inner diameter expansion (i.e., smallest pattern allowances) occurred at the mid-height of the cylinder. This resulted in a barrel-shaped profile along the inner diameter's height, which can be explained by local solidification times. The ends of the cylinder solidified relatively fast, which reduced the duration of core expansion (recall that the core only expanded during solidification).
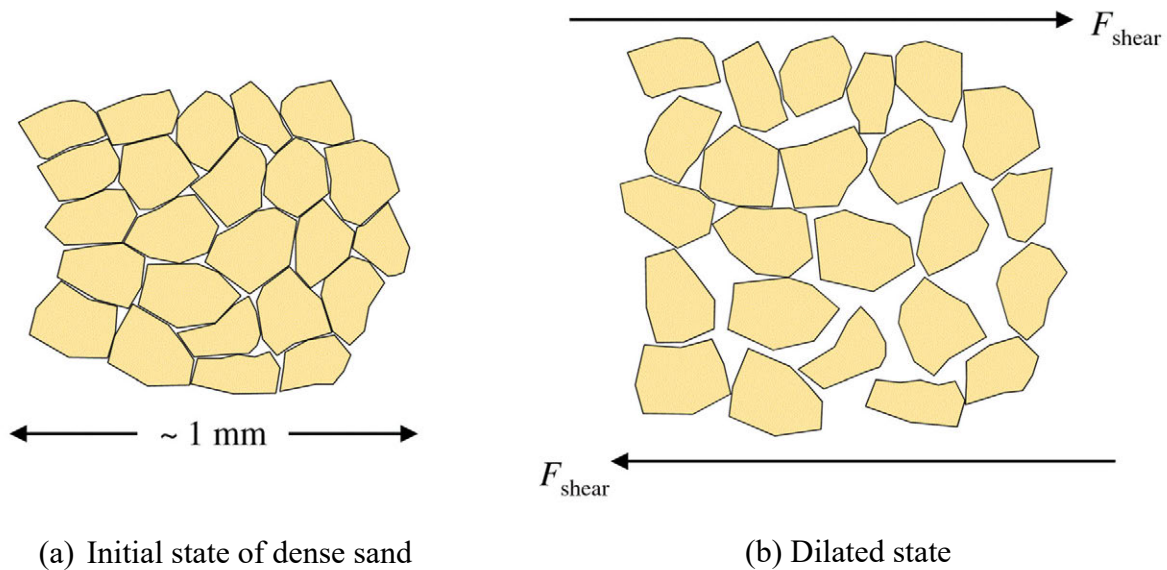

(a) Initial state of dense sand (b) Dilated state

Figure 7. Dense sand dilates (i.e., volumetrically expands) when subjected to a shear force, F_{shear}, due to void growth between grains.
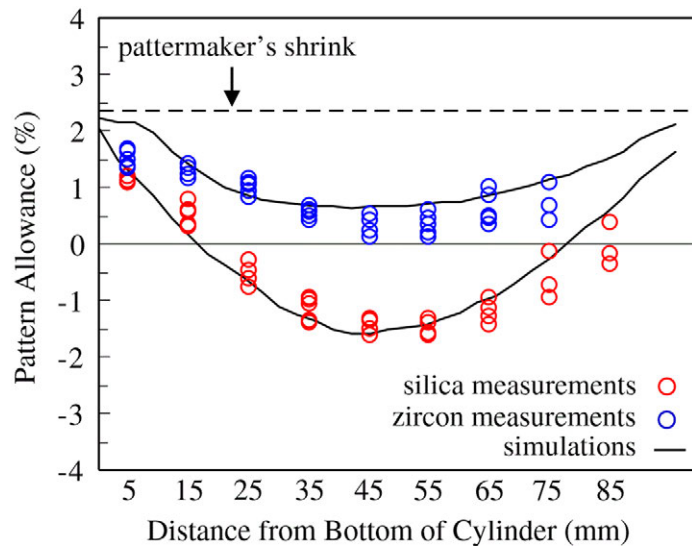
Figure 8. Final comparison between measured and predicted pattern allowances for the silica and zircon core experiments.

Despite its findings, Reference [9] calibrated a constitutive model for bonded sand only at early times, i.e., before complete solidification. Indeed, mold restraint after solidification can also generate considerable distortions throughout the casting. In order to calibrate the sand model after solidification, Galles and Beckermann [10] cast a U-shaped bracket using the geometry and experimental setup shown in Figure 9. Note that the "outer

(a) Casting geometry
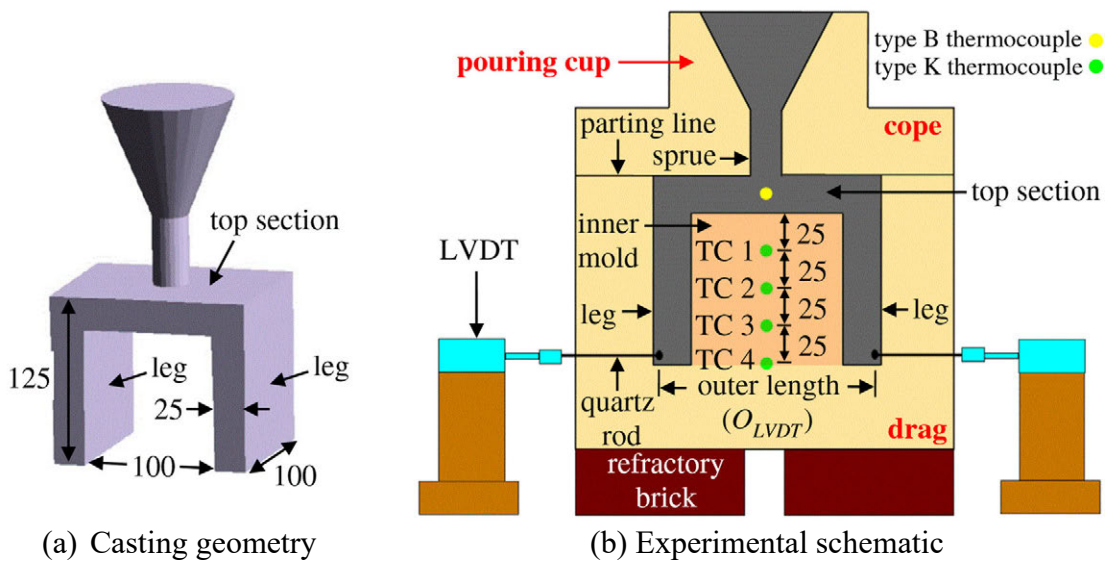
(b) Experimental schematic

Figure 9. Casting geometry (a) and experimental schematic (b) for the bracket experiments. All dimensions are in mm.
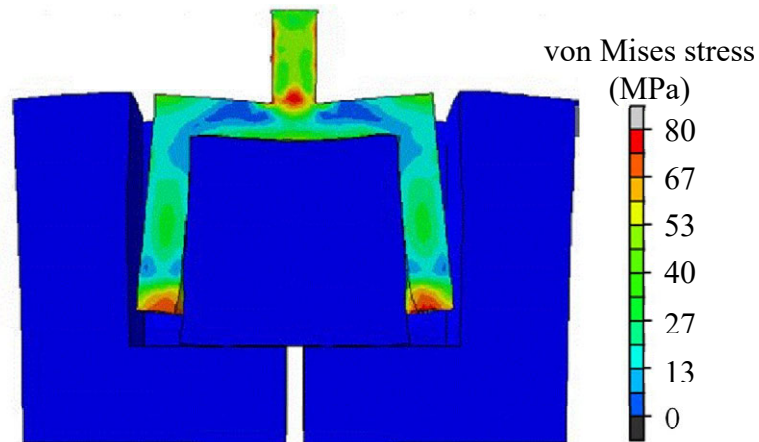
Figure 10. Predicted von Mises stresses in the bracket. Distortions are magnified 5x.

length" dimension in Figure 9(b) was used to characterize distortions for this study. During

the experiments, thermal contractions in the bracket were restrained by the inner mold. As

a result, the bracket legs distorted outward. A simulation of this behavior is shown in Figure

10, which also reveals separation of the outer mold. Shortly after solidification, stresses in

the outer portion of the mold led to fracture at its mid-plane. Unless a fracture plane was

incorporated into the simulation model, the outer mold restrained the pushout of the bracket

legs, resulting in the under-prediction of distortions. In general, the measured distortions

varied between the experiments, as shown in Figure 11. In particular, the change in outer
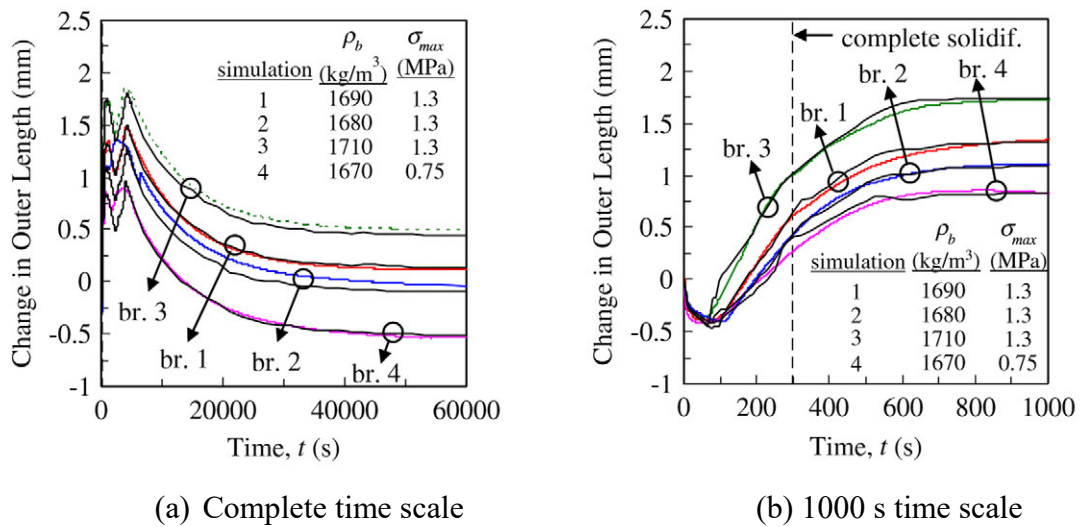

(a) Complete time scale

(b) 1000 s time scale

Figure 11. Comparison between the measured and predicted (black curves) changes in outer
length after adjustments to the packing density (ρ_b) and tensile strength (σ_{max}) of the mold.

length at 1000 s ranged from 0.8 to 1.75 mm (see Figure 11(b)). In order to predict these differences, the packing density (ρ_b) and tensile strength (σ_{max}) of the mold were adjusted for each experiment. The sensitivity of predicted distortions on packing density (which ranged from 1670 – 1710 kg/m^3) is remarkable. Such a result demonstrates the importance of consistent mold packing. By matching the simulated and measured evolution of the outer length for each experiment, the pattern allowances at the feature locations in Figure 12(a) were also predicted accurately (see Figure 12(b)), regardless of the wide range of measurements (-2% < PA < 6%).Through the findings of [9] and [10], a constitutive model for bonded sand was calibrated.

Once models for the steel and sand were calibrated, Galles and Beckermann [12] demonstrated the predictive capability of the model through a case study. A dimensional analysis for a production steel casting was provided from an industry partner, for which pattern allowances were measured at the ten feature locations shown in Figure 13.
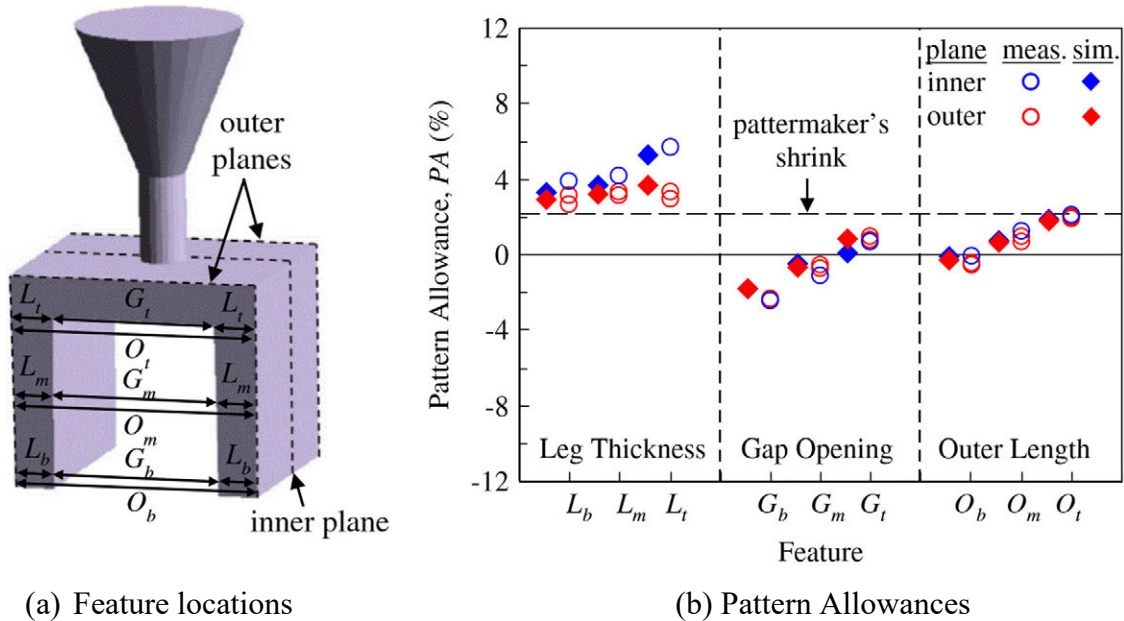

(a) Feature locations

(b) Pattern Allowances

Figure 12. Comparison between the measured and predicted pattern allowances.
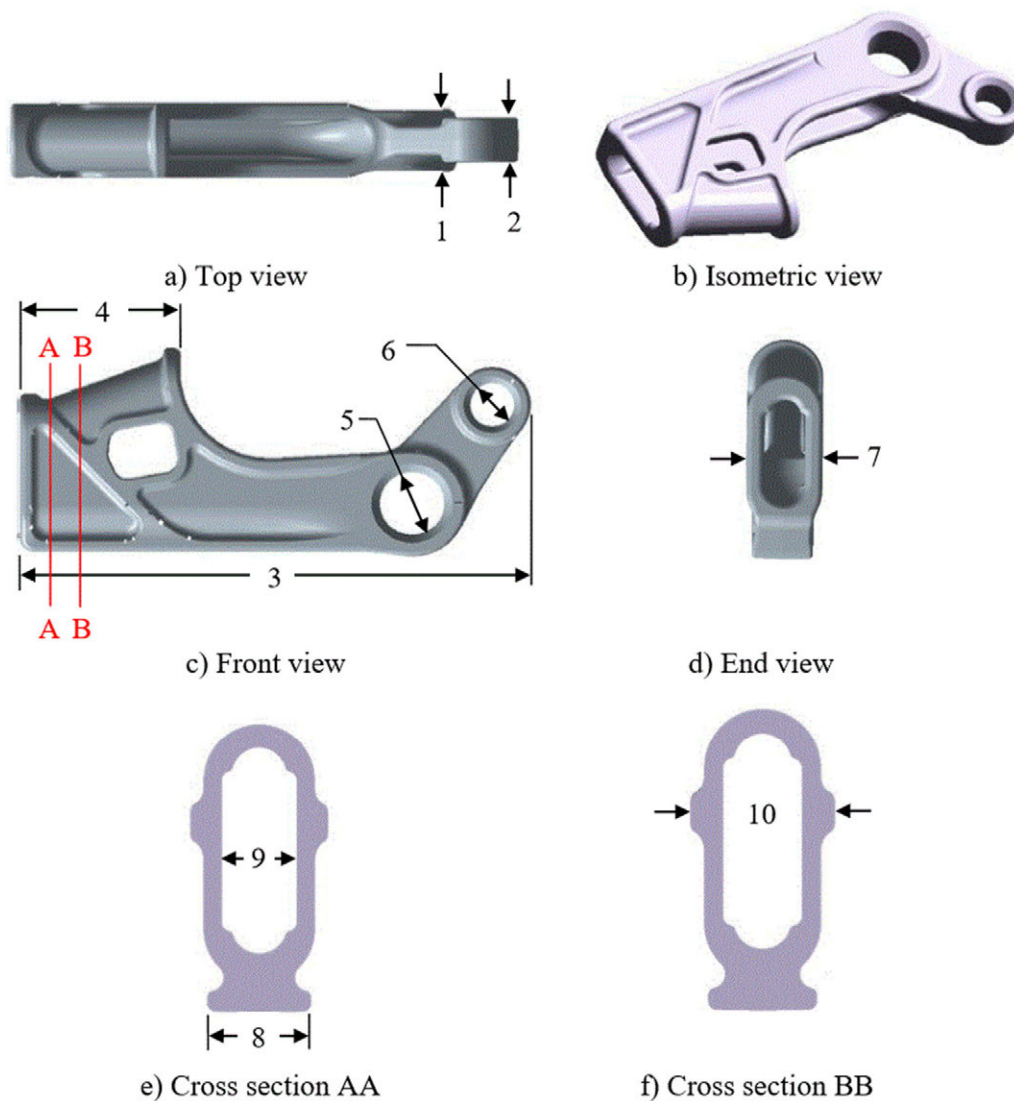
Figure 13. Casting geometry and feature lengths for production steel casting.

This analysis revealed a range distortions, some of which were both greater than and less than the free shrink pattern allowance (2.1%). Nonetheless, the FEM simulation predicted these distortions with good accuracy, as illustrated by the bar graph in Figure 14. The distorted shape calculated by the simulation is shown in Figure 15, which overlays the transparent pattern shape to aid in visualization.

The aforementioned studies revealed several important findings. By incorporating these findings into the computational model, it was demonstrated that the FEM simulations
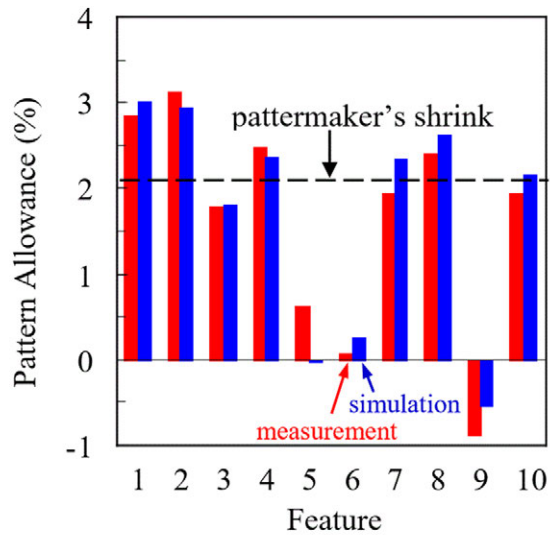
Figure 14. Comparison between the measured and predicted pattern allowances for the features shown in Figure 13.
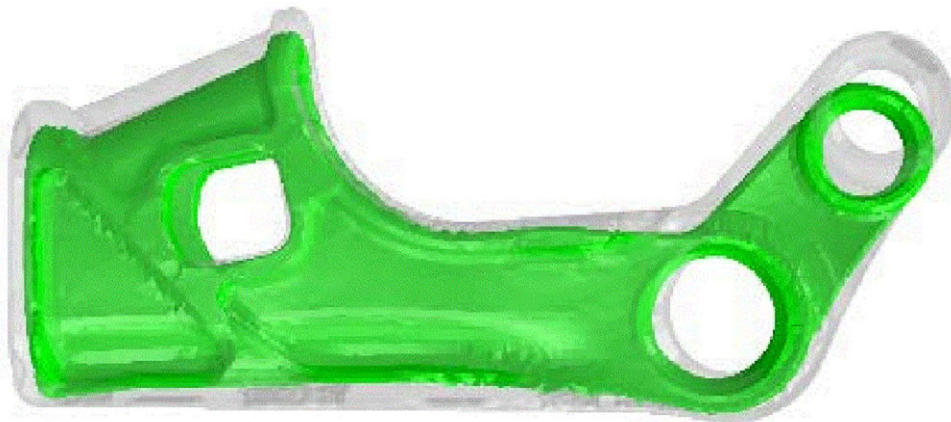

Figure 15. The distorted shape at room temperature was calculated by the FEM simulation and is overlaid on the pattern shape. Distortions are magnified 5x.

can accurately calculate distortions for castings of arbitrary size and shape. It is envisioned that studies such as these will incite confidence for computer simulation and ultimately spur the transition from physically to digitally-based pattern design.

3. Inverse elastoplastic problem and properties

The inverse elastoplastic problem presented in this section calculates the pattern geometry from the known as-cast shape. The model reviewed here is the general quasi-static formulation presented by Lu and Li [6] with the following simplifications. Due to

the relatively small casting sizes, body forces will have a negligible impact on distortions and therefore, are not considered. Also, the exclusion of the mold from the mechanical problem precludes the need to include surface tractions in the formulation. These simplifications reduce the boundary value problem to

$$
\sigma_{ij,j} = 0 \ \text{in} \ \Omega
$$
$$
\boldsymbol{\Phi} = \overline{\boldsymbol{\Phi}} \quad \text{on} \ \partial\Omega_u
$$

(1)

where σ_{ij} is the Cauchy stress and $\overline{\boldsymbol{\Phi}}$ is a prescribed displacement on boundary $\partial\Omega_u$. Eq. 1 determines an inverse motion $\boldsymbol{\Phi} : \Omega \to B \in R^3$ for the sought reference configuration, B, when starting from the given current configuration, Ω. Stated another way, the inverse deformation $\boldsymbol{\Phi}(\mathbf{x}, t)$ describes the correspondence between the current coordinate $\mathbf{x}$ and its reference coordinate $\mathbf{X}$. Such a relation is the kinematic inverse of the usual forward deformation $\varphi(\mathbf{X}, t)$ of a material point that progresses from the reference coordinate to the current coordinate. Similarly, the inverse deformation gradient $\mathbf{f} = \partial_{\mathbf{x}} \boldsymbol{\Phi}(\mathbf{x}, t)$ is the kinematic inverse of the forward deformation gradient $\mathbf{F} = \partial_{\mathbf{X}} \varphi(\mathbf{X}, t)$. Additional details, including the finite element implementation, can be found elsewhere [6].

During the inverse solution procedure, the material response obeys a Hencky constitutive relation, which is very close to a linear elastic response at small strains, provided the stress levels do not exceed the yield strength of the casting. For the elastic properties, a constant value of 0.3 was specified for Poisson's ratio and a temperature-dependent Young's modulus, shown in Figure 16(a), was taken from Koric and Thomas [13]. For the case of yielding, the following elasto-plastic constitutive relation is invoked:

$$
\sigma = \sigma_0 \left(1 + \varepsilon_p\right)^n
$$

(2)

where σ is the von Mises stress, σ_0 is the initial yield stress, ε_p is the equivalent plastic strain, and n is the hardening exponent. Eq. 2 is a simplified form of the elasto-visco-plastic constitutive relation used by Galles and Beckermann [8] to calculate stresses and
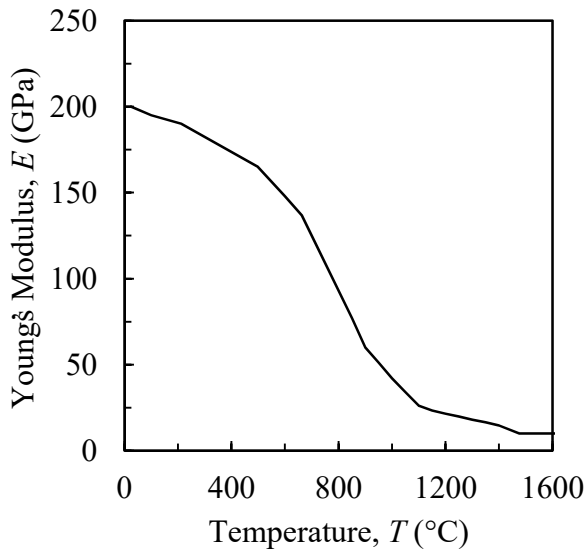
(a) Young's Modulus
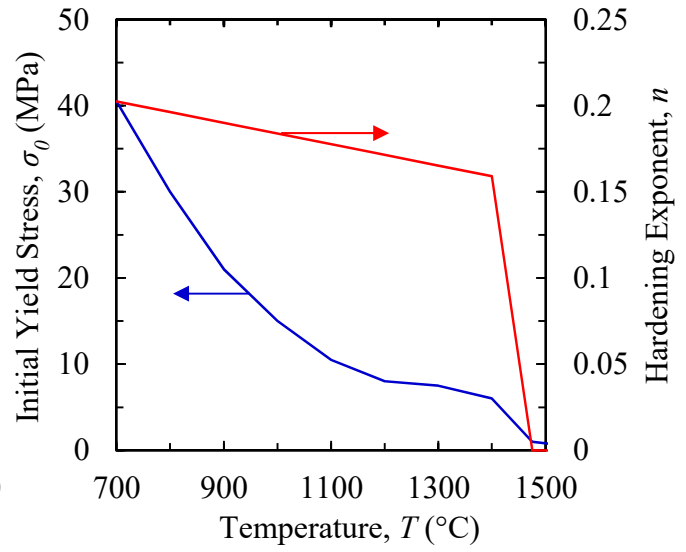
(b) Initial Yield Stress and Hardening Exponent
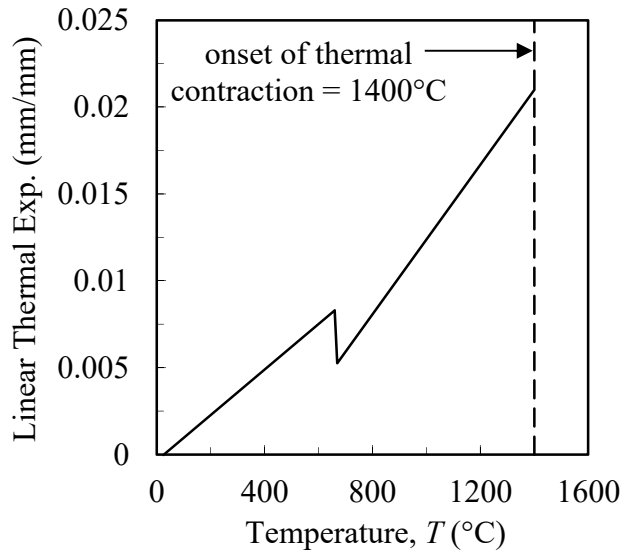
(c) Linear Thermal Expansion

Figure 16. Inputs for the stress analysis included Young's Modulus (a), the linear thermal expansion for steel (b), and the initial yield stress and hardening exponent (c).

distortions during steel casting. The simplification involves using a representative constant strain rate to replace the rate dependent term in the original elasto-visco-plastic relation. The remaining temperature-dependent model parameters (σ_0 and n) in Eq. 2 were determined using a Levenberg-Marquardt non-linear least squares algorithm and are shown in Figure 16(b). A sufficient number of data points for this algorithm were generated at various temperatures from the calibrated model of Galles and Beckermann [8] using a representative strain rate of 1×10^{-5} s^{-1}. Since the constitutive parameters were based on a previously calibrated casting model, the simulations in this study can be expected to give reasonable predictions. Thermal strains were calculated using the temperature-dependent linear thermal expansion coefficient shown in Figure 16(c). This curve was calibrated from the thermal contraction data of an unrestrained steel bar [8].

4. Numerical examples

4.1   Introduction

Casting processes occur over large temperature ranges, which induce thermal strains that may lead to considerable stresses and associated distortions. As previously stated, the present study only considers thermal stresses that are created by uneven cooling in the casting and not mechanical stresses caused by contact interactions between the casting and mold. For simple casting geometries without internal features (e.g., holes), minimal mechanically-induced distortions can be expected after solidification, as the casting quickly gains the necessary strength to prevent any distortions created by mold-metal interactions [9]. This rationale motivated the designs of the bar and plate casting geometries shown in Figure 1(a) and 1(b), respectively. Dimensions in the figures are shown in mm. For the bar, preliminary heat transfer simulations revealed nearly constant cooling. Therefore, a chill was added to the bottom of the bar in order to generate directional cooling and induce ample thermal stresses. Such a strategy was not needed for the plate casting system, whose inclusion of simplified risers and a gating system produced

the varying section thicknesses necessary to naturally create uneven cooling.

The numerical examples presented in this section were conducted utilizing a sequential thermal-mechanical coupling. Heat transfer simulations were performed first to calculate the transient temperature fields, which were then used as inputs for the forward and inverse stress analyses. A loop test served to evaluate the inverse method. For this test, the inverse analysis was performed first to determine the pattern shape, which was subsequently used as the input geometry for the forward analysis. Validation of the inverse technique is based on the loop test's ability to recover the initial geometry used for the inverse analysis.

4.2   *Heat transfer simulations*

Spatial temperature gradients (i.e., uneven cooling) within the castings are essential for this study because they drive the thermal loading that generates distortions. Without them, deformations caused only by stress-free thermal contractions, in which case all dimensions will adhere to the patternmaker's shrink rules. Temperature fields were calculated using the casting simulation software MAGMASOFT® [7]. In order to generate realistic casting temperatures, the bonded sand mold was included in the simulation model. Simulation inputs included thermophysical properties for the mold and casting, solid volume fraction during solidification, and latent heat of solidification. In addition, the interfacial heat transfer coefficient must be specified. This parameter accounts for the air gap formation between the casting and mold and thus, allows for decoupling of the thermal-mechanical problem. All inputs, excluding the latent heat of solidification, are temperature-dependent. The calibration procedure for the current heat transfer model, as well as the aforementioned inputs, can be found in Galles and Beckermann [14]. Due short pour times, mold filling had a negligible impact on the calculated casting temperatures and therefore, was not included in the simulations.

Temperature fields at various times are shown at the mid-plane of the bar and plate

castings in Figure 17. For the bar casting (see Figure 17(a)), the calculated temperatures are nearly isothermal at $t = 10$ s. At $t = 41$ s and $t = 60$ s, however, chill-induced spatial temperature gradients that are mostly parallel to the horizontal plane can be seen. It will be shown in the following section that these gradients generated a bending moment in the bar. After only $t = 1$ min 32 s, however, the gradients are much less prominent, as temperatures tend towards an isothermal state. Finally, at $t = 4$ min 6 s, temperature variations can no longer be seen in the bar. Consequently, minimal bending of the bar caused by thermal stresses can be expected after this time.

Due to its larger size, the cooling times in the plate casting are significantly longer than those in the bar, as shown in Figure 17(b). Regardless, spatial temperature gradients can again be seen throughout the casting, most notably at $t = 5$ min and $t = 21$ min. After these times, the plate temperature fields are nearly isothermal. Contrary to the bar casting, however, variations in section thickness throughout the plate geometry naturally induced spatial temperature gradients. In particular, the risers are chunky and formed hotspots that cooled slowly. Conversely, the gating cross section is small in comparison to the other components of the casting system and therefore cooled relatively fast. This observation is notable, because the cooling patterns in the plate casting will closely resemble those that can be expected in a production casting. Thus, Figure 17(b) illustrates how essential components of a casting system (e.g., gating and risers) inherently generate uneven cooling that can lead to distortions.

The calculated temperature fields were written at a sufficient number of time steps to ensure a smooth temperature profile at all material points. The results were then copied onto the finite element mesh used for the stress analysis.
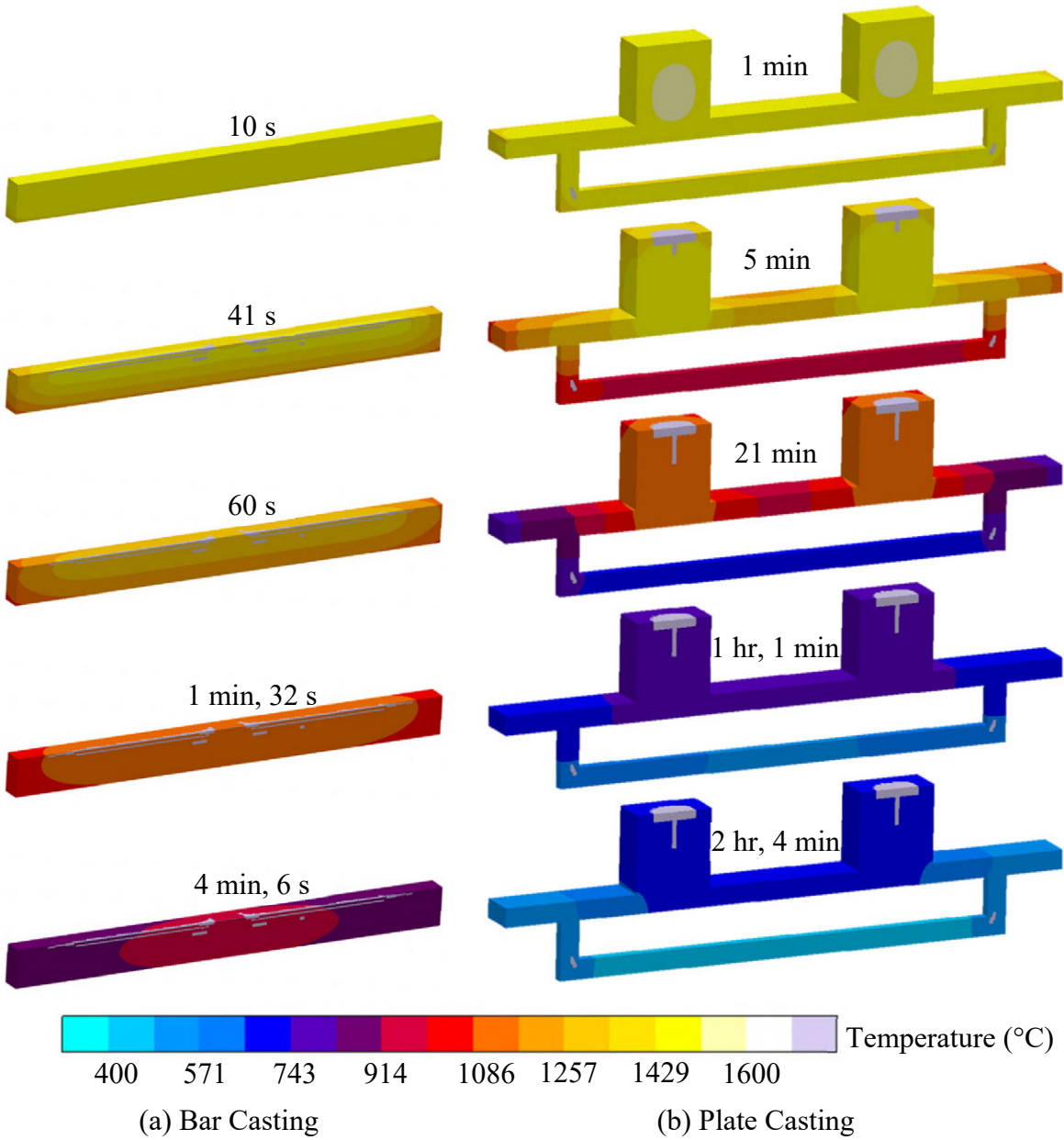
Figure 17. Predicted temperatures at the casting mid-plane are shown at various times for the bar (a) and plate (b) castings.

4.3   *Stress simulations*

3D Stress simulations were performed using the general purpose finite element code FEAP. In order to prevent rigid body translations and rotations, minimal boundary conditions were specified at the mid-length of both castings, which assured symmetric

deformations about the casting mid-plane. Due to its larger size, advantage was taken of the plate symmetry and only ¼ of the geometry was modeled. First order brick elements were used for the simulations.

Loop tests were conducted to evaluate the inverse solution. These tests involved performing an inverse stress analysis first in order to determine the pattern geometry, which was then used as the input geometry for the forward stress analysis. If successful, the forward analysis will recover the initial geometry used for the inverse analysis within a reasonable level of accuracy. Both analyses commence from an initial state without stresses or plastic deformations and are prescribed the same loading (i.e., thermal) history.

In order to quantify differences between the forward and inverse analyses, the following metrics were adopted. A configuration error, $err\,(conf\,)$, evaluated differences between calculated inverse and forward displacements and was computed by normalizing differences in the current position $\mathbf{x}$ by the forward displacement $\boldsymbol{u}$:

$$err(conf)[\%] = \frac{\int_\Omega \left\| \mathbf{x}^{Inverse} - \mathbf{x}^{Forward} \right\| dv}{\int_\Omega \|\boldsymbol{u}\| dv} \times 100 \tag{3}$$

In Eq. 3, $\mathbf{x}^{Inverse}$ refers to the input geometry for the inverse simulation, whereas $\mathbf{x}^{Forward}$ relates to the calculated coordinates of the forward simulation. In addition, a scaled error norm, $err\,(\cdot)$, was computed for the equivalent plastic strain and von Mises stress using the following relation:

$$err(\cdot)[\%] = \frac{\int_\Omega \|\Delta(\cdot)\| dv}{\int_\Omega \|(\cdot)\| dv} \times 100 \tag{4}$$

In Eq. 4, $(\cdot)$ represents the quantity of interest (i.e., equivalent plastic strain or von Mises stress) calculated from the forward analysis and $\Delta(\cdot)$ is the difference between the forward and inverse solutions.

In addition to the computed errors, the final vertical profile of the casting's top edge

is plotted to help the reader visualize the deformations. Also, the temporal evolution of vertical displacement for a single point located at the upper left corner of each casting is plotted.

3.3.1   Bar casting

The loop test for the bar casting commenced with an inverse analysis, which calculated the configuration shown in Figure 18(a). Distortions are enhanced 20x to aid visualization. Recall that the input casting geometry for the inverse simulation is shown in Figure 1(a). Although it was not included in the stress analysis, the chill induced uneven cooling that led to an upward distortion of the bar ends. Keep in mind that this deformation was calculated within the inverse framework and is therefore reverted. In reality, the ends of a physical bar produced under the present conditions will distort downward. This behavior is easily confirmed through a forward stress analysis. In a similar vein, the usual thermal contractions that occur during casting are manifested as expansions for the inverse problem. For example, the calculated bar length in Figure 18(a) spans from -153.15 mm to 153.15 mm, a total of 306.3 mm. This value exceeds the input geometry length by 6.3 mm and corresponds to the unrestrained (i.e., free shrink) pattern allowance of 2.1% for a low allow steel. Thus, the inverse technique accounts for both mechanical and thermal strains to determine a pattern shape that can be expected to produce the as-cast geometry shown in Figure 1(a). For the second part of the loop test, the pattern shape determined by the inverse analysis (Figure 18(a)) was used as the input geometry for the forward analysis, which then calculated the shape shown in Figure 18(b). This configuration appears to be similar to the original input geometry shown in Figure 1(a) that was inputted into the inverse analysis.

The calculated bar configurations in Figures 18(a) and 18(b) were further analyzed by plotting the vertical position of the bars' top edges as a function of axial position in Figure 18(c). The reference lines in Figures 18(a) and 18(b) represent the zero vertical

(a) Inverse Analysis

(b) Forward Analysis
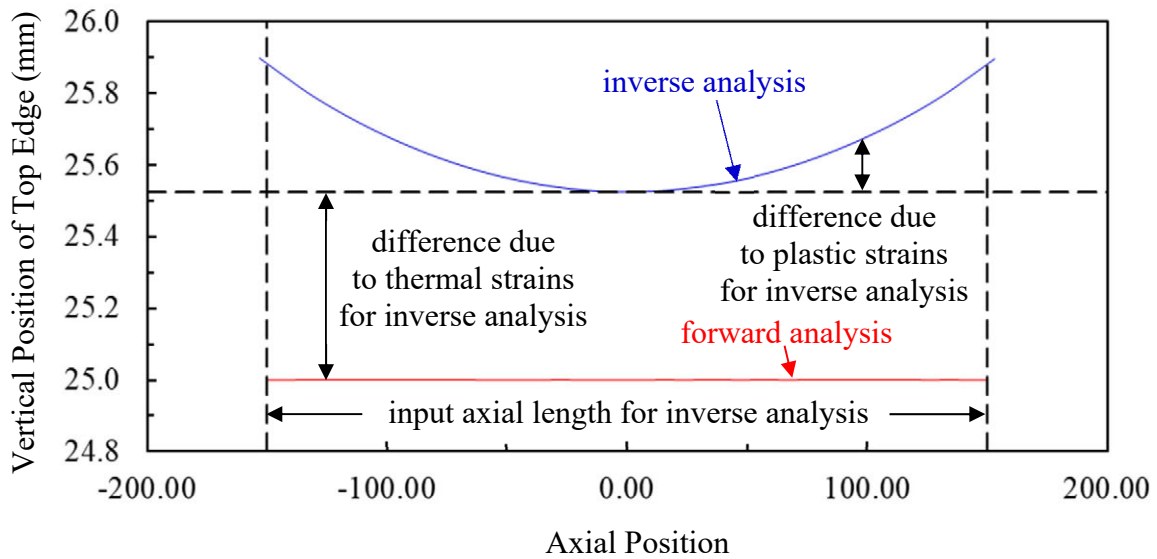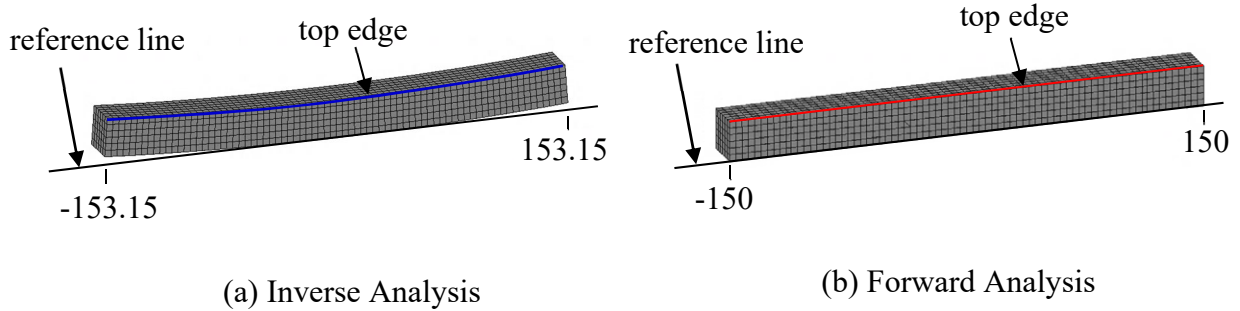
(c) Predicted Vertical Position at Top Edge of Bar

Figure 18. Bar configurations calculated by the inverse (a) and forward (b) simulations. The vertical position along the top edge of the bars is plotted as a function of axial position in (c). A 20x deformation factor is used in (a) and (b).

position. For the inverse analysis (blue curve), the top edge generally increases from an initial constant vertical position of 25 mm, which corresponds to the input geometry shown in Figure 1(a). This increase is due to a combination of thermal strains and distortions. The horizontal dashed line in Figure 18(c) represents the vertical increase of the top edge due to thermal strains for the inverse analysis. Deviations from this line represent distortions, which increase monotonically from zero at axial position = 0 to a maximum value at the bar ends. The increased bar length calculated by the inverse analysis due to thermal strains

is also apparent in Figure 18(c), as the inverse analysis curve extends beyond the two vertical dashed lines that represent the original bar length.

The most important takeaway from Figure 18(c) is that the configuration calculated by the forward analysis recovers the top edge dimensions of the bar geometry inputted into the inverse analysis. Specifically, the 300 mm bar length and constant vertical profile of 25 mm for the top edge is identical for both geometries. Since the deformation for the bar is relatively simple, recovery of the top edge can be expected to result in recovery for the rest of the bar.

The temporal evolution of vertical displacement for a single point at the upper left corner of the bar is plotted on complete (30,000 s) and 200 s time scales in Figures 19(a) and 5(b), respectively. These plots demonstrate that for all times, the inverse and forward evolutions are equal in magnitude but opposite in sign. Thus, at any given time step, the forward calculation recovers the original geometry used for the inverse simulation. The forward curve provides a physical interpretation of the evolution (recall that the inverse simulation produces unphysical results). The forward curve begins to decrease downward at approximately 10 s and reaches a minimum value of -2.15 mm at 45 s. This sharp downward deflection is due to rapid cooling and solidification at the bottom of the casting, which is not only accompanied by an increase in strength but also triggers the onset of thermal contraction. Meanwhile, the upper portion of the bar is still mostly liquid and therefore, relatively weak. As a result, thermal contractions in the bottom portion of the bar create a bending moment that easily distorts the bar ends downward while also plastically deforming solidified regions in top of the bar. As the solidification front progresses upward, the upper portion of the bar gains strength and also begins to thermally contract. This counteracts the bending moment that caused the initial downward distortion. Consequently, the bar ends deflect upward, which is seen as an increase in vertical displacement from 45 s to approximately 150 s. After 150 s, small negative changes in forward displacement are due to additional thermal strains, as minimal temperature gradients at these later times
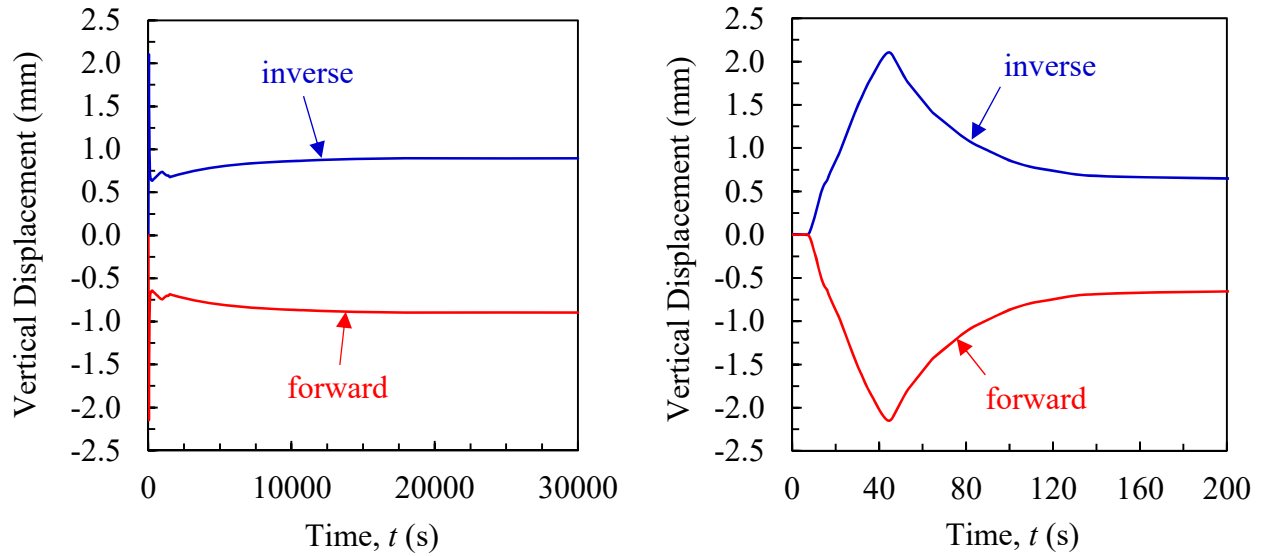
(a) Complete time scale

(b) 200 s time scale
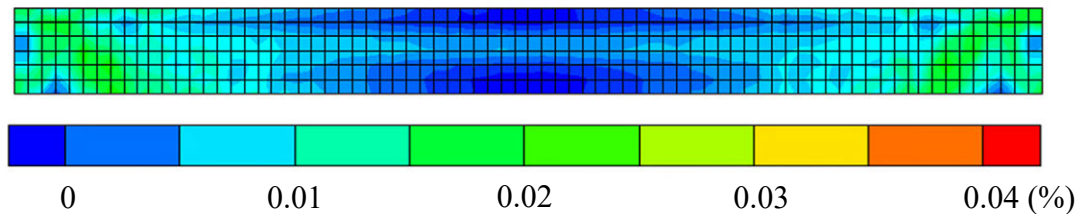
(c) Configuration error

Figure 19. Vertical deflection at the upper left corner of the bar plotted as a function of time on complete (a) and 200 s (b) time scales. The configuration error is shown in (c).

cannot generate the thermal loading needed to produce distortions. The final bar shape is characterized by a slight downward distortion at its ends, which is manifested as a negative vertical displacement at 30,000 s for the forward curve. This final shape was anticipated due to the generation of plastic strains at early times that increased the length at the top of the bar and prevented the bar ends from returning to their original vertical position. An additional feature of the curves in Figure 19(a) is the small "wiggle" seen at 1000 s, which is attributed to a brief volumetric expansion that accompanies the decomposition of austenite to ferrite and cementite.

The elemental configuration error is shown on a contour map in Figure 19(c). The largest errors are seen at the ends of the bar, which correspond to the regions of largest deformation. However, the maximum configuration error for the bar is less than 0.04%. Furthermore, the average configuration error over the entire bar geometry is 0.01% (see Table 1). Such small differences in configuration can be neglected for all practical purposes. Accordingly, the loop test validates the finite inverse deformation analysis for the bar casting.

Contour plots of von Mises stress and equivalent plastic strain are plotted for the inverse and forward simulations and are shown with their associated errors in Figure 20. Errors are shown on the desired as-cast configuration. In general, the von Mises stress and equivalent plastic strain contour maps are similar for both for the forward and inverse simulation. The maximum error values are 6.9% and 1.5% for the von Mises stress and equivalent plastic strain, respectively. However, the average respective errors over the entire domain are only 0.23% and 0.29% for von Mises stress and equivalent plastic strain.

Table 1. Average errors of configuration, equivalent plastic strain, and von Mises stress.

Case	err(conf)	err(ep)	err(qv)
Bar	0.01%	0.29%	0.23%
Plate	1.78%	2.38%	6.56%

3.3.2 Plate casting

The bar casting in the previous section was shown to recover the desired as-cast shape through successive inverse and forward stress simulations. Such a simple geometry, however, is not representative of a typical foundry casting. In reality, casting systems contain features (e.g., gating, risers) that inherently create complex geometries, which in turn may lead to uneven cooling that generates distortions. Therefore, the plate casting

(a) Inverse von Mises Stress

(b) Inverse Equivalent Plastic Strain

(c) Forward von Mises Stress

(d) Forward Equivalent Plastic Strain

(e) von Mises Stress Error

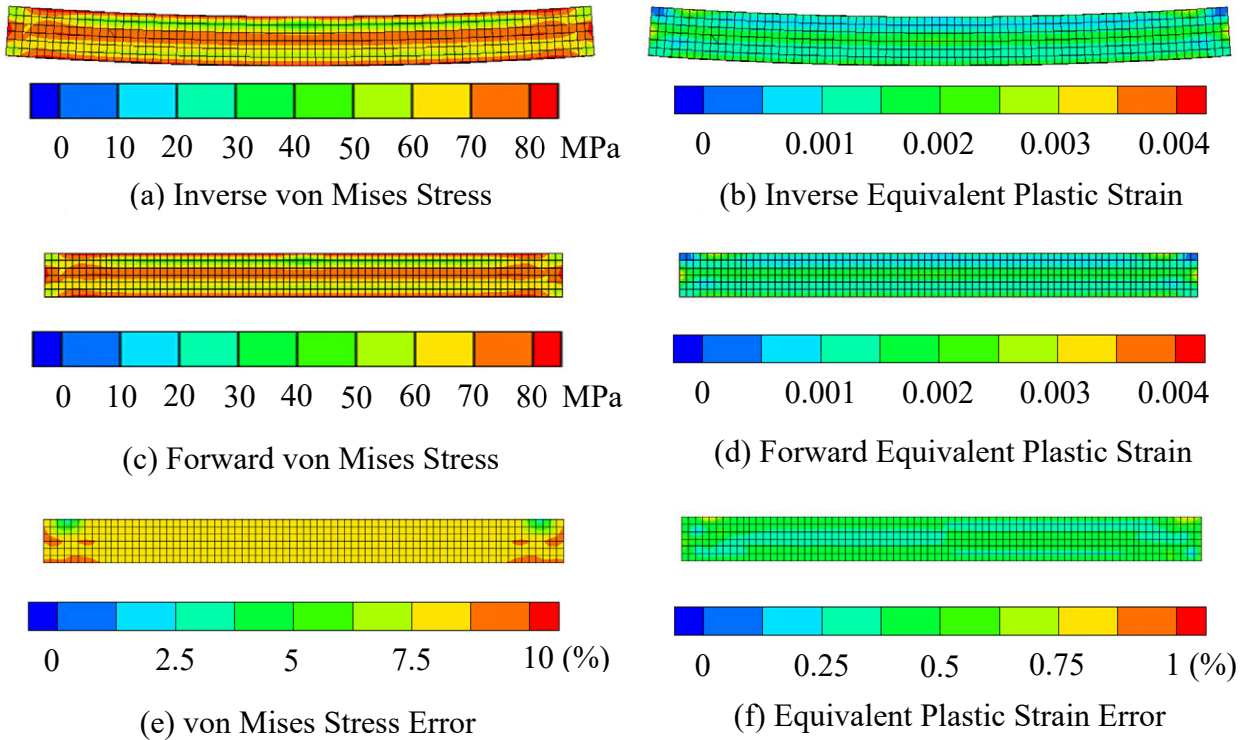(f) Equivalent Plastic Strain Error

Figure 20. Von Mises stresses, equivalent plastic strains, and associated errors for the bar. A 20x deformation factor is used in (a) and (b).

model in Figure 1(b) was created to provide a realistic (albeit simplified) casting system to which the finite element inverse deformation analysis could be applied.

The inverse analysis was again performed first. It was previously shown during the heat transfer analysis that the gating and risers naturally created uneven cooling and associated thermal loading for the plate casting system. Such loading resulted in the calculated configuration shown in Figure 21(a). Since deformations were symmetric about the vertical plane, only one half of the geometry is shown. In general, the deformation behavior for the plate resembles that of the bar. Specifically, 1) the ends of the plate are distorted upward and 2) the casting length increases. The upward distortion is expected because the cooling trends are the same for both castings, i.e., the bottom cools faster than the upper portion of the casting. The length increase, as previously discussed, is due to calculation of thermal strains in the inverse framework. In addition to distortions in the

plate, the gating is also distorted upward at its mid-length. Despite this additional complexity, the configuration calculated by the forward simulation (see Figure 21(b)) once again recovers the input geometry that was used for the inverse analysis. The final vertical displacement at the top edge for both configurations is plotted as a function of axial position in Figure 21(c). As in the bar example, thermal and plastic strains cause the vertical position of the top edge to evolve from a constant vertical height of 25 mm to the profile shown by the blue curve for the inverse simulation. The forward simulation subsequently recovers the constant vertical profile of 25 mm, as demonstrated by the red curve in Figure 21(c).
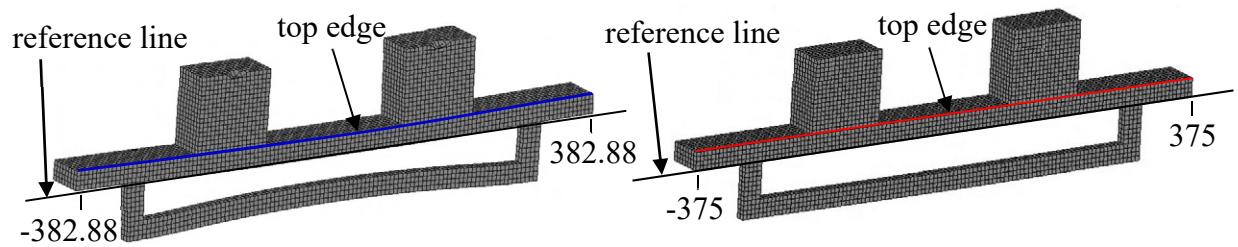
(a) Inverse Analysis

(b) Forward Analysis
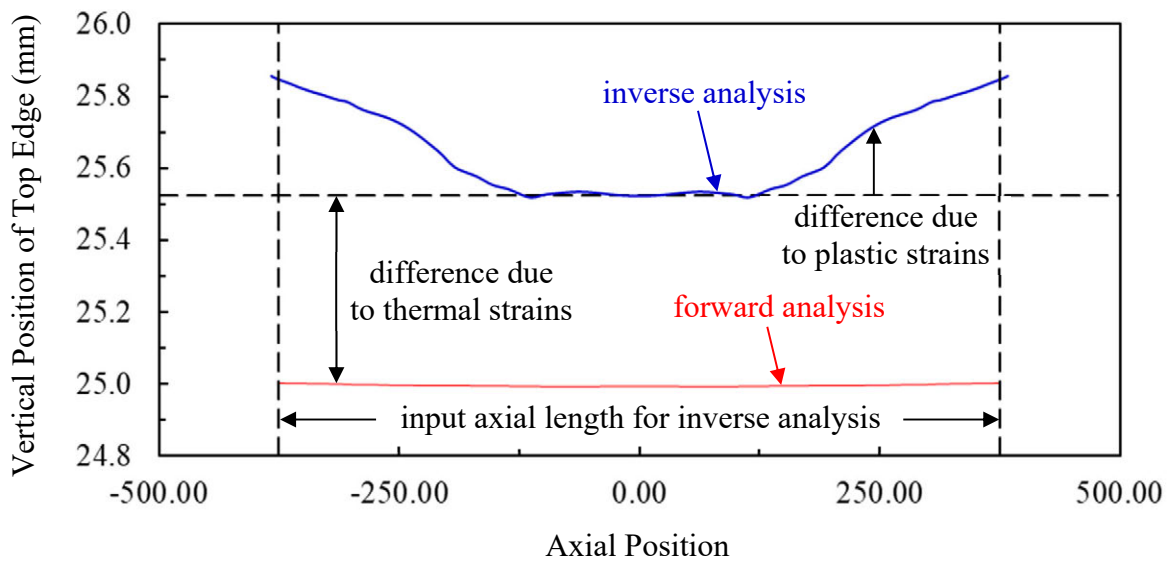
(c) Predicted Vertical Position at Top Edge

Figure 21. Plate configurations calculated by the inverse (a) and forward (b) simulations. The vertical position along the top edge of the plates is plotted as a function of axial position in (c). A 10x deformation factor is used in (a) and (b).

The temporal evolution of vertical displacement for a point at the top left corner of the plate is plotted on complete (80,000 s) and 5000 s time scales. Although the time scales and magnitudes of displacement are different, characteristic features of these plots resemble those of the bar casting. In particular, the initial decrease in forward displacement (to a minimum value at 675 s) is followed by an increase (until approximately 5000 s), after which the decomposition of the austenite phase is accompanied with a volumetric expansion that causes the plate ends to displace downward (from 5000 s to 8000 s). After the phase transformation is complete, additional thermal contractions cause the plate ends to gradually displace upward until 80,000 s. The configuration error shown in Figure 22(c)

(a) Complete time scale

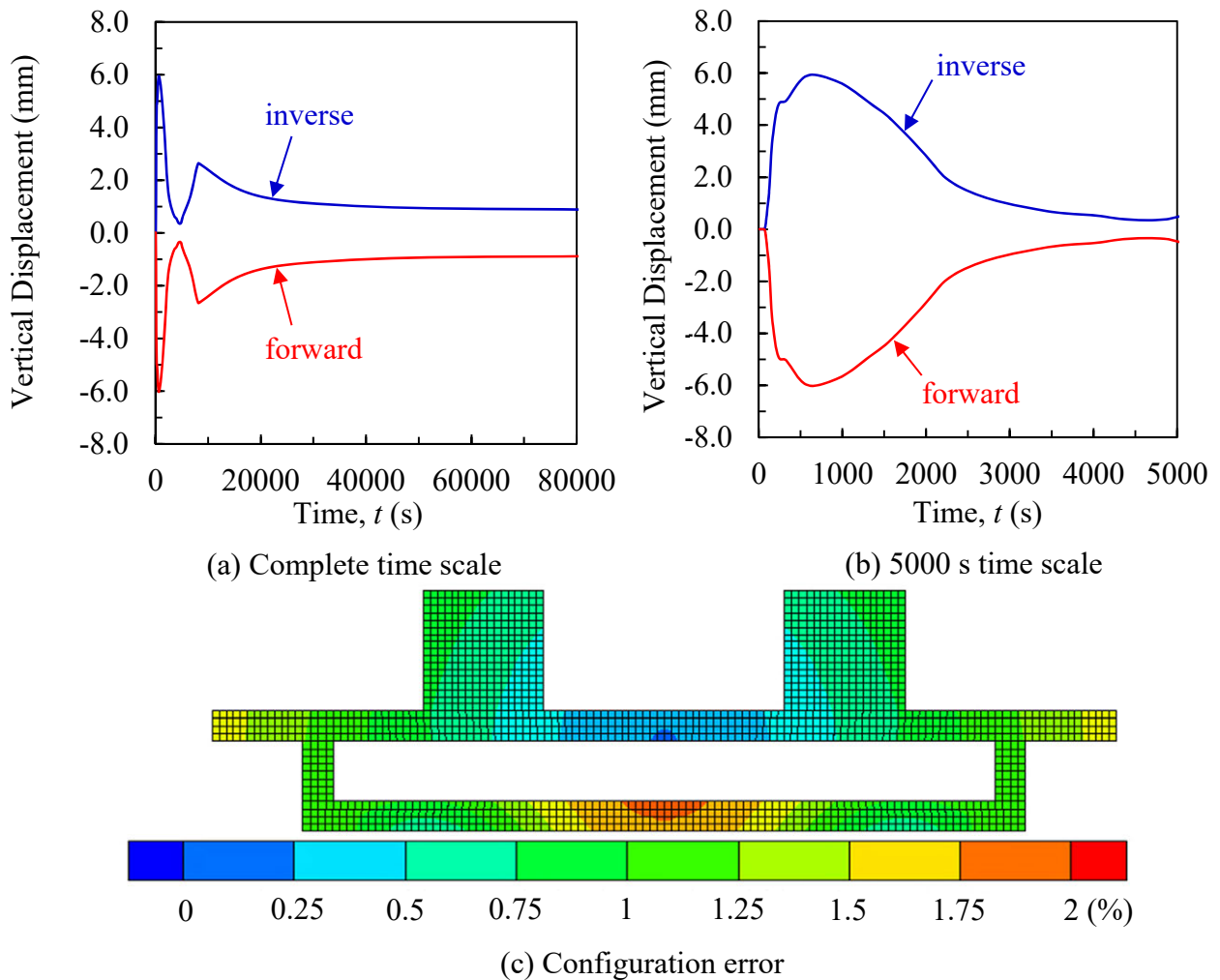(b) 5000 s time scale

(c) Configuration error

Figure 22. Vertical deflection at the upper left corner of the plate plotted as a function of time on complete (a) and 5000 s (b) time scales. The configuration error is shown in (c).

is larger than that for the bar but still reasonably small ($< 2\%$). The average configuration error for the entire plate casting system (1.78%) is summarized in Table 1.

Contours of von Mises stress, equivalent plastic strain, and associated errors are shown in Figure 23. Errors are plotted on the desired as-cast configuration. Although the forward and inverse contours again appear to contain no discernable differences, the error calculations reveal local differences that are less than 10% and 4% for von Mises stress and equivalent plastic strain, respectively. The average errors over the domain, shown in Table 1, are 6.56% and 2.38% for von Mises stress and equivalent plastic strain, respectively.

(a) Inverse von Mises Stress

(b) Inverse Equivalent Plastic Strain

(c) Forward von Mises Stress

(d) Forward Equivalent Plastic Strain

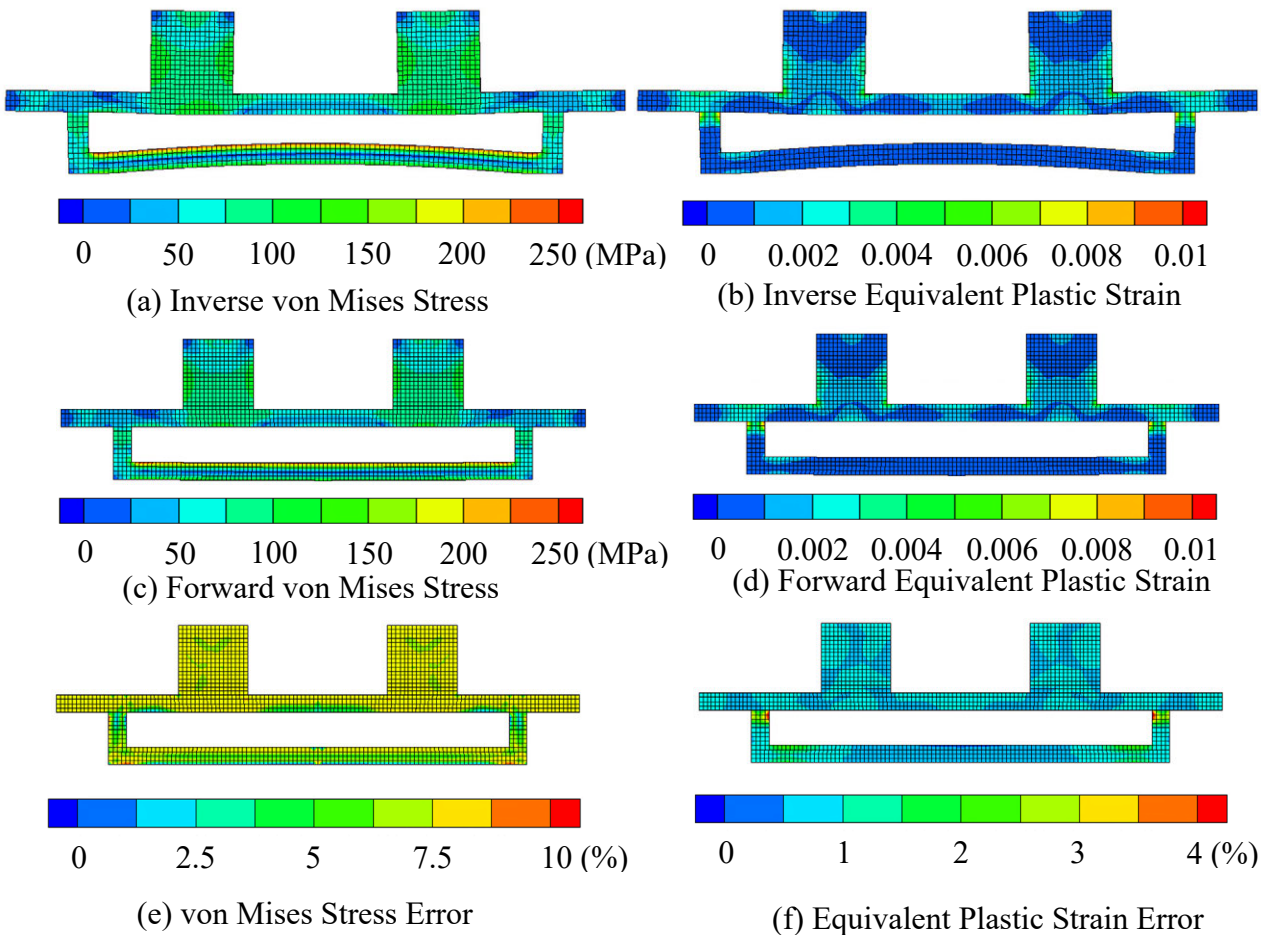(e) von Mises Stress Error

(f) Equivalent Plastic Strain Error

Figure 23. Von Mises stress, equivalent plastic strains, and associated errors for the plate casting. A 10x deformation factor is used in (a) and (b).

In general, the computed errors for the bar were smaller than those for the plate. A likely explanation for this difference can be found by comparing the maximum vertical deflection at the ends of the castings. The end of the bar and plate castings distort to maximum absolute values of 2.15 mm (at 45 s) and 5.93 mm (at 675 s), respectively (see Figures 19(b) and 22(b)). Therefore, the material points for the plate generally traveled a larger displacement path than those for the bar. For this reason, larger errors can be expected in the plate casting. Regardless, the configuration errors for both castings are reasonably small, as the finite inverse deformation analysis calculated pattern shapes with excellent accuracy.

5. Conclusions

Casting distortions arise during metalcasting and create dimensional inaccuracies in the as-cast part. Their presence necessitates a costly trial-and-error pattern design process that extends lead times and reduces efficiency. The present study explores the viability of the finite element inverse deformation analysis to calculate pattern allowances for steel castings. The underlying concept behind this technique involves finding, by solving a boundary value problem, a deformation that is the kinematic inverse of that for the usual forward analysis. As a result, the inverse analysis essentially works backward, starting from the desired as-cast configuration, to determine pattern dimensions in a single design iteration.

The inverse deformation analysis was evaluated through a loop test, which involved performing an inverse simulation first using the desired as-cast configuration as input. The resulting calculated pattern shape was then inputted into a forward analysis, which attempted to recover the original geometry used for the inverse analysis. An important caveat for this recovery concerns the elastoplastic constitutive relation used in this study. The calculation of plastic deformations will generally lead to different loading paths between the forward and inverse problems. However, since plastic strains (i.e., distortions)

for casting processes are typically on the order of a few percent, only marginal differences were expected between the inverse and forward loading paths. This was indeed the case for the plate casting system, which contained a moderately complex geometry and deformation history. Nonetheless, the loop test accurately recovered the original geometry, as the average difference between inverse and forward configurations was less than 2%.

The finite element inverse deformation analysis potentially provides an efficient means to calculate pattern dimensions. Although this study represents an important step towards achieving this goal, further work is needed before this technique can be applied to production castings. Primarily, mechanical interactions between the casting and mold must be considered. Currently, the numerical difficulties associated with contact interactions prompted the authors to only consider distortions caused by thermal stresses. Overcoming this issue is paramount to the success of the inverse deformation analysis. It should also be noted that accuracy of the inverse analysis was evaluated based on comparisons to the forward analysis. Thus, the importance of the forward simulation's predictive capability cannot be overstated. The present material model is based one that was previously calibrated for a low alloy steel using in situ data from casting experiments. If the finite element inverse deformation analysis is used for other casting materials, care must be taken to properly calibrate the associated material model parameters for the forward problem. Despite these concerns, the present results lend confidence to the inverse deformation analysis for its ability to ultimately determine pattern allowances accurately and with unprecedented efficiency.

Acknowledgements

Laboratory or the U.S. Government. The U.S. Government is authorized to reproduce and distribute reprints for Government purposes notwithstanding any copyright notation herein.

References

1. Yamada T. Finite element procedure of initial shape determination for rubber-like materials. Technical Report no. 20, Res. Lab Eng. Mat. Tokyo Inst. Tech.;1995.

2. Govindjee S, Mihalic PA, Computational methods for inverse finite elastostatics. *Comput. Methods Appl. Mech. Eng.* 1996;136:47-57.

3. Lu J, Li L. On referential and spatial formulations of inverse elastostatic analysis. *Comput. Methods Appl. Mech. Eng.* 2016;310:189–207.

4. Germain S, Steinmann P, Menary G. On inverse form finding for anisotropic elastoplastic materials. *AIP Conference Proceedings-American Institute of Physics.* 2011;1353:1169-1174.

5. Germain S, Scherer M, Steinmann P. On a recursive formulation for solving inverse form finding problems in isotropic elastoplasticity. *Adv. Model. Simul. Eng. Sci.* 2014;1:1–10.

6. Lu J, Li L. Determining the reference geometry of plastically deformed material body undergone monotonic loading and moderately large deformation. *Finite Elements in Analysis and Design.* 2017;130:1-11.

7. Magma GmbH, MAGMAsoft, Kackerstrasse 11, 52072. Aachen, Germany.

8. Galles D, Beckermann C. In situ measurement and prediction of stresses and strains during casting of steel. *Metall. Mater. Trans. A.* 2016;47A:811-829.

9. Galles D, Beckermann C. Effect of sand dilation on distortions and pattern allowances during steel sand casting. *Int. J. Cast Metals Res.* 2017;30:257-275.

10. Galles D, Beckermann C. Simulation of distortions and pattern allowances for a production steel casting. *Proceedings of the 69th SFSA Technical and Operating Conference*, paper no. 3.7, Chicago (IL), Steel Founders' Society of America; 2015.

11. Wray PJ. Effect of carbon content on the plastic flow of plain carbon steels at elevated temperatures. *Metall. Mater. Trans. A.* 1982;13A(1):125-134.

12. Galles D, Beckermann C. Simulation of distortions and pattern allowances for a production steel casting. *Proceedings of the 69th SFSA Technical and Operating Conference*, paper no. 3.7, Chicago (IL), Steel Founders' Society of America; 2015.

13. Koric S, Thomas BG. Thermomechanical finite-element model of shell behavior in continuous casting of steel. *Int. J. Numer. Methods Eng.* 2006;66:1955-1989.

14. Galles D, Beckermann C. Measurement and prediction of stresses during casting of a steel bar. *Proceedings of the 65th SFSA Technical and Operating Conference*, paper no. 5.5, Chicago (IL), Steel Founders' Society of America, Chicago; 2011.